Journal of Materials Chemistry A

PAPER

View Article Online
View Journal | View Issue

Cite this: J. Mater. Chem. A, 2014, 2, 3834

Supercapacitors with high capacitance based on reduced graphene oxide/carbon nanotubes/NiO composite electrodes†

Yang Bai, Meng Du, Jie Chang, Jing Sun* and Lian Gao

Received 3rd December 2013
Accepted 5th January 2014

DOI: 10.1039/c3ta15004f

www.rsc.org/MaterialsA

We present a facile method to fabricate well-crystalline reduced graphene oxide (RGO)/carbon nanotubes (CNTs)/NiO composites for supercapacitor electrodes. The RGO/CNT/NiO (GCN) composite takes dual advantages of CNTs and RGO. CNTs present the aggregation of RGO/NiO and improve the electron transport of GCN composites owing to their good conductivity. The restricting effect of RGO makes NiO nanoparticles have more active sites. Attributed to the uniform structure and improved electrical conductivity, GCN composites exhibit highly enhanced electrochemical performance compared with that of RGO/NiO and CNT/NiO composites. The specific capacitance of GCN composites is about 1180 F g^{-1} at 1 A g^{-1} together with a capacitance retention of 95% (1000 F g^{-1}) over 2000 cycles at 4 A g^{-1}. GCN composites have proven to be very promising as energy storage electrode materials.

1. Introduction

Electrochemical capacitors (ECs) are novel energy storage devices with high power performance, long cycle life, and low maintenance cost.[1–3] Usually, ECs show higher power density and longer cycle life but lower energy density than batteries. They are appropriate for devices which require short-term power or act as peak power assistances for batteries.[3,4] According to different energy storage mechanisms of electrode materials,[5–7] ECs could be classified into two types, electric double layer capacitors (EDLCs) and pseudo-capacitors (PCs). EDLCs store energy *via* ion adsorption processes and PCs *via* fast surface redox reactions.[8–10] Carbon materials, such as active carbon (AC), carbon nanotubes (CNTs), and graphene, have large specific surface area, excellent electrical conductivity and high power density for EDLCs.[11–13] However, their energy densities are limited by the adsorption capacity for electrolyte ions. On the other hand, pseudo-capacitive materials include transition metal oxides/hydroxides[14–17] and conducting polymers.[18] They can provide multiple redox reactions to obtain higher capacitance values. Unfortunately, low electric conductivities of these materials limit electron transport,[2] leading to low power densities. A major challenge in this field is to improve energy densities of ECs and simultaneously retain their high power densities.

NiO, a typical pseudo-capacitive material with high theoretical capacity, is easy to synthesize with low cost.[14] It has attracted a great deal of attention to be applied in PCs. Zhang *et al.* synthesized porous NiO nanocolumns with a relatively high specific capacitance (390 F g^{-1}) than those of other morphologies.[19] Cao *et al.* fabricated flowerlike NiO hollow nanospheres, showing a high specific capacitance of 585 F g^{-1}.[20] Although NiO has shown a relatively high capacitance, its electron and ion transport abilities are low. Apart from designing the morphology of NiO, many efforts[21–23] have been focused on combining NiO and carbon materials to improve the conductivity.

Graphene is one of the most promising carbon materials due to its excellent electrical and mechanical properties. Among various preparation methods, chemical reduction of graphene oxide (GO) is considered as the most convenient method for bulk production.[24–26] The high surface area and electrical conductivity enable the chemical derived reduced graphene oxide (RGO) to modify electrochemical materials. Zhu *et al.* prepared a RGO/NiO electrode with a high specific capacitance of 770 F g^{-1} and enhanced rate capability.[27] Zhao *et al.* studied the electrochemical properties of monolayer graphene/NiO nanosheets, which showed a high specific capacitance of 525 F g^{-1}.[28] The electrochemical performance of these RGO based composites is significantly enhanced compared with those of pure NiO. However, the residual oxygen-containing functional groups in RGO, poor crystallinity and nonuniform structure would reduce the stability of these RGO based electrodes. Besides, RGO/NiO composites will restack easily due to the intensive π–π interaction during the reaction process,[29] which will also shorten the cycle life of the electrodes. These issues urgently need to be solved.

The State Key Lab of High Performance Ceramics and Superfine Microstructure, Shanghai Institute of Ceramics, Chinese Academy of Sciences, 1295 Dingxi Road, Shanghai 200050, P.R. China. E-mail: jingsun@mail.sic.ac.cn; liagao@mail.sic.ac.cn; Fax: +86-21-52413122; Tel: +86-21-52414301

† Electronic supplementary information (ESI) available: Fig. S1 and Table S1. See DOI: 10.1039/c3ta15004f

Carbon nanotubes (CNTs) are widely used carbon materials to improve the conductivity of transition metal oxides.[3,30,31] Ni–Co oxide/CNT composites synthesized by Fan *et al.* showed a high specific capacitance of 569 F g^{-1}, as well as a good cycle life.[32] Liu *et al.* fabricated CNT/NiO/Ni nanocomposites with a high specific capacitance and excellent capacitive behavior.[28] All these results certified that CNTs were appropriate for improving the electron transport of composite electrodes. However, their poor solubility and tendency towards aggregation are not beneficial for metal oxide anchoring. Consequently, the interfacial bonding between CNTs and metal oxides is weak, leading to inferior stability of the electrodes. As far as we know, graphene oxide can improve the dispersion of CNTs, which preserves the electronic structure of CNTs and forms a better conductive network.[29]

Inspired by this phenomenon, we synthesized RGO/CNT/NiO (GCN) composites *via* a simple method under mild conditions. In the synthesis process, urea was used to control the hydrolysis of metal salts and reduce GO to RGO. The reagents used in this process were environmental friendly. The aggregation of RGO/NiO was successfully avoided by the addition of CNTs. The sizes of NiO particles were decreased and the conductivity of GCN composites was enhanced because of the synergistic effect of RGO and CNTs. As a consequence, GCNs showed a high specific capacitance of 1180 F g^{-1} at 1 A g^{-1}. The capacitance at 4 A g^{-1} was still as high as 1000 F g^{-1} with the loss rate of 5% after 2000 cycles, certifying excellent cycling stability. GCN composites have proven to be very promising as energy storage electrode materials.

2. Experimental section

2.1 Material preparation

Graphite was purchased from Alfa Aesar (325 mesh). Carbon nanotubes were purchased from Shanghai Chenrong electric furnace Co., Ltd. All of the other chemical reagents used in our experiments are of analytical grade, purchased from Shanghai Sinopharm Chemical Reagent Co., Ltd. (Shanghai, China). Graphene oxide (GO) was prepared from graphite flakes by a modified Hummers method.[33] The as-prepared GO was dispersed in distilled water by ultrasonication, forming a yellow-brown suspension with a concentration of 1 mg mL^{-1}. Carbon nanotubes (CNTs) used in this work were pretreated with nitric acid (analytical grade). The as-received CNTs were firstly refluxed with 60% (w) HNO_3 solution at 80 °C for 6 h, then washed with distilled water and dried.

2.2 Synthesis of RGO/CNT/NiO composites

In a typical process, 0.02 g as-received CNTs was added into an 80 mL GO suspension with a concentration of 1 mg mL^{-1} under vigorous stirring. Then, 50 mL aqueous solution containing 0.4362 g $Ni(NO_3)_2 \cdot 6H_2O$ and 1.5 g urea was slowly dropped into the GO and CNTs suspension. After stirring for 30 min, the mixture was refluxed at 100 °C for 12 h in an oil bath. The reaction product was filtered and washed with distilled water and ethanol successively several times. Finally, it was dried at 60 °C overnight and then heat treated at 250 °C for 2 h in air. The obtained RGO/CNT/NiO composite powder was denoted as GCN. With the other conditions being the same, 100 mg CNTs or GO were used as the carbon source to replace GO/CNTs. The reaction products were denoted as CNO and GNO, respectively.

2.3 Characterization

Powder X-ray diffraction (XRD, Rigaku D/Max 2200PC, Cu Kα) was used to characterize the crystalline structure. Raman spectroscopy was recorded on a DXR Raman Microscope with an excitation length of 532 nm. X-ray photoelectron spectroscopy (XPS) analysis was conducted using a twin anode gun, Mg Kα (1253.6 eV) (Microlab 310F Scanning Auger Microprobe, VG SCIENTIFIC Ltd). The morphology and structure of the products were analyzed on a field-emission scanning electron microscope (FE-SEM, Magellan 400) and a transmission electron microscope (TEM, JEOL JEM-2100F).

The electrochemical properties of the materials were characterized using a three-electrode system in 2 M KOH aqueous solution at room temperature. The working electrode was prepared as follows. 4 mg of CNO, GNO or GCN active materials, 0.5 mg of carbon black and 0.5 mg of polyvinylidene fluoride (PVDF) binder were mixed in ethanol, and then pasted onto a nickel foam current collector. Each working electrode weighed 5 mg. Platinum wire was used as the counter electrode and Hg/HgO as the reference electrode. The electrochemical impedance spectrum (EIS) was tested by applying an AC voltage with 5 mV amplitude in a frequency range from 0.01 Hz to 100 kHz on a CHI660D Workstation (Shanghai, China). The cyclic voltammetry (CV) at −0.1 to 0.65 V was performed on a CHI660D Workstation. The galvanostatic charge and discharge tests were carried out in the potential range of 0.1–0.6 V on a LAND CT2001 battery tester. The specific capacitances C_s were calculated from the galvanostatic discharge curves using the equation:[5,34]

$$C_s = \frac{it}{(\Delta v)m} \quad (1)$$

where i, t, Δv, and m are the constant current (A), discharge time (s), potential drop during discharge (V), and mass of active materials (g), respectively.

3. Results and discussion

The XRD patterns of as-prepared CNTs (a), CNO (b), GNO (c), and GCN (d) are illustrated in Fig. 1. Two obvious peaks with 2θ values of 25.74° and 42.89° in the as-prepared CNT sample are the characteristic peaks of the (002) and (100) planes,[35,36] respectively. The diffraction peak of CNTs at 25.74° is also observed in CNO and GCN samples. The diffraction peaks of NiO are found in CNO, GNO, and GCN samples at 37.24°, 43.28°, and 62.88°, which are in well agreement with the standard diffraction card of face-centered-cubic NiO (JCPDS card no. 47-1049). However, NiO peaks in GNO are imperfect, corresponding to poor crystallinity. For the GO sample, a diffraction peak at 12.16° is consistent with (001) reflection, and after

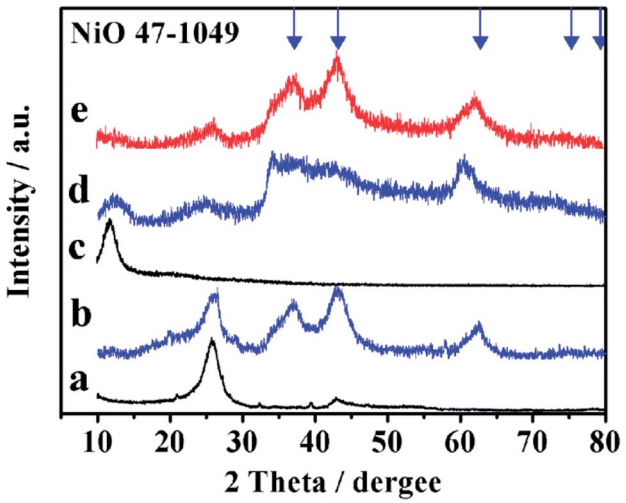

Fig. 1 XRD patterns of as-prepared CNTs (a), CNO (b), GO (c), GNO (d), and GCN (e).

reduction, the characteristic peak of carbon from RGO could be found around 24.5°.[37–39] In the GNO sample, two peaks observed at 12.26° and 24.51° are associated with GO and RGO, respectively. But, no peak of GO is displayed in the GCN sample. Further examination with XPS illustrates the reduction degree of RGO. In the high-resolution C1s XPS spectra of GO, GNO, and GCN (Fig. S1†), the absorbance band intensities of C–O and C(O)O in GO are much weaker in comparison with their counterparts in GNO and GCN. The ratios of C–O and C(O)O in GCN are much lower than those of GNO, indicating a high reduction degree of GO in GCN.

Raman spectra are used to analyze the physical structure of carbon in these samples (Fig. 2). The G band (~1590 cm^{-1}) is attributed to the vibration of sp^2-bonded carbon atoms, while the D band (~1350 cm^{-1}) arises from the disorders or defects and the 2D band at ~2700 cm^{-1} originates from a double-resonance process.[40–43] Distinctive D and G bands around 1350 cm^{-1} and 1590 cm^{-1} are observed in all samples. The 2D bands are only found in the samples with CNTs, indicating the intact tube structure of CNTs.[44] The intensity ratio of the D/G band (I_D/I_G) will increase when the structure defect increases.[25,45] The I_D/I_G ratio is 0.56 in CNTs, exhibiting fewer structure defects. After compositing with NiO, more defects are induced during the synthesis process. Thus the I_D/I_G ratio increased to 0.72 in CNO. I_D/I_G ratios are 0.99, 1.10, and 0.87 in GO, GNO, and GCN, respectively. When GO is reduced to RGO, oxygen-containing functional groups are removed. Though the conjugated graphene network is reestablished, the size of the reestablished graphene network is usually smaller than the original graphene layer, resulting in the increase of I_D/I_G ratio.[46] Therefore, the increase of I_D/I_G ratio from 0.99 to 1.10 is reasonable. However, the I_D/I_G ratio in GCN is lower than that in GNO, showing fewer structure defects. It is probably because the reduction of RGO in GCN is better than that of GNO and partial GO is substituted with CNTs, which would decrease the concentration of defects in GCN.

SEM was carried out to characterize the structures of different samples. Fig. 3 shows SEM images of CNO (a and b), GNO (c and d), and GCN (e and f) composites. CNTs and flake-like NiO are mixed together, as seen from Fig. 3a. NiO sheets with a size of 100–200 nm are twined by CNTs irregularly (Fig. 3b). As exhibited in Fig. 3c, NiO and RGO are heavily aggregated in GNO, which will lead to a decreased specific area. RGO sheets still have a flake-like structure (Fig. 3d). In Fig. 3e and f, both RGO sheets and CNTs could be observed. A majority of small NiO slices are anchored on the surfaces of RGO sheets, which are separated by CNTs with less aggregation. In comparison with CNO and GNO, GCN composites are less aggregated with more active sites exposed. CNTs insert into the

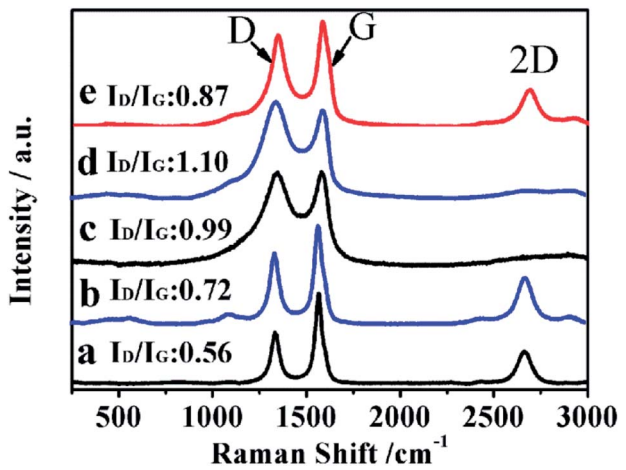

Fig. 2 Raman spectroscopy of as-prepared CNTs (a), CNO (b), GO (c), GNO (d), and GCN (e).

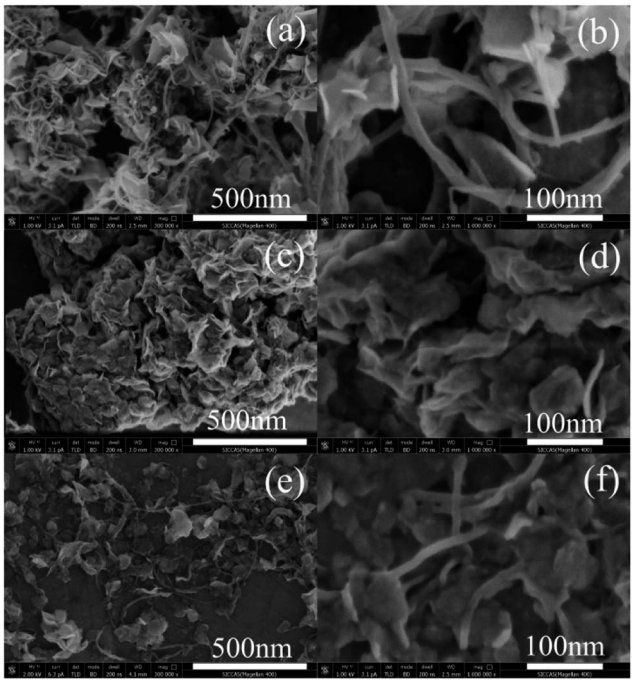

Fig. 3 SEM images of the CNO (a and b), GNO (c and d), and GCN (e and f).

interlayer of RGO as a skeleton structure to support RGO sheets and prevent them from aggregation. Meanwhile, CNTs provide the tunnels for electron transport. Thus, a good electrical conductivity is expected.

To further analyze the microstructure of CNO (a and d), GNO (b and e), and GCN (c and f) composites, TEM images were taken. As shown in Fig. 4a, paper-like NiO sheets with large size are dispersed on the surface of CNTs in CNO samples. CNTs provide a good skeleton structure to support NiO, which prevents the severe aggregation of NiO nanoflakes. By contrast, RGO anchored with NiO particles aggregated into the bulk in GNO samples (Fig. 4b). The aggregation is caused by the intensive π–π interaction between RGO sheets. In GCN samples (Fig. 4c), NiO particles are anchored onto RGO sheets. They are connected by CNTs and form continuous network. CNTs help to avoid the aggregation among sheets. More active sites are available and electron transport properties will be improved in GCN. Crystallinities of these samples are illustrated in HRTEM images. Lattice fringes of NiO in CNO are clear and long (Fig. 4d), testifying the good crystallinity and large size of NiO. Oppositely, lattice fringes of NiO could be hardly observed in GNO samples (Fig. 4e). Only some short and dim fringes can be found, corresponding to the poor crystallinity of NiO as described in XRD

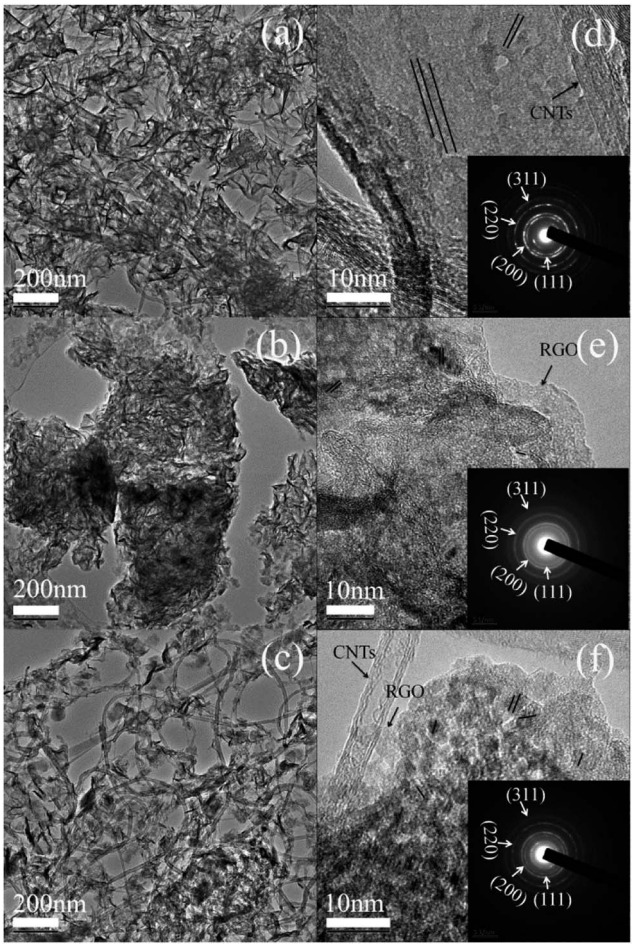

Fig. 4 TEM images of the CNO (a and d), GNO (b and e), and GCN (c and f).

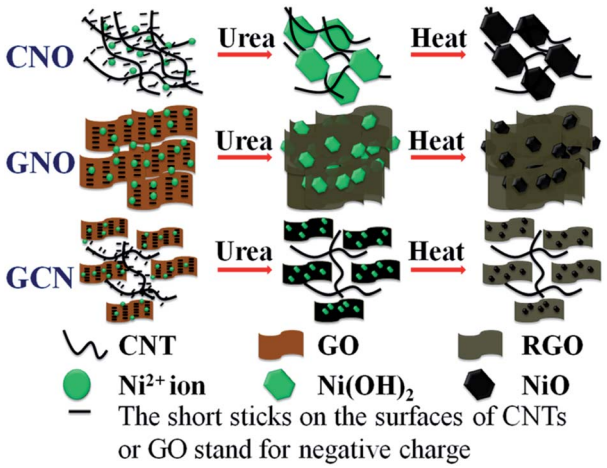

Fig. 5 Schematic illustrations of the synthesis process of CNO, GNO, and GCN.

analysis. In Fig. 4f, clear and short fringes indicate high crystallinity and decreased particle size of NiO in GCN. The selected area electron diffraction (SAED) results show that NiO in all the composites is polycrystalline with a cubic structure.

On the basis of the above results, the synthetic processes of CNO, GNO and GCN composites are proposed as follows (Fig. 5). For CNO, negatively charged CNTs[47] attract Ni^{2+} ions by electrostatic forces. Then, Ni^{2+} ions combined with OH^- provided by the hydrolyzation of urea to form $Ni(OH)_2$. With the increase of time at high temperature, the particle size of $Ni(OH)_2$ grows larger. It is probably due to the poor solubility and tendency towards aggregation of CNTs, which could not restrict the growth of $Ni(OH)_2$ particles. For GNO, a similar process occurred. Ni^{2+} ions were attracted onto the negatively charged GO surfaces[48] and formed $Ni(OH)_2$ nanoparticles. The growth of $Ni(OH)_2$ particles is limited by the restricting effect of RGO, so the particle size of $Ni(OH)_2$ decreased in comparison with those in CNO. GNO restacked after reduction due to the intensive π–π interaction. For GCN, CNTs and GO, both negatively charged, are dispersed homogeneously in the solution. Ni^{2+} ions will be attracted and anchored on GO preferentially due to their large specific surface areas. $Ni(OH)_2$ formed with small size in GCN due to the restricting effect of RGO and transformed into NiO during the heat treatment process.

The electrochemical properties of the materials were characterized by CV and galvanostatic charge and discharge measurements. Fig. 6a presents the CV curves of CNO, GNO, and GCN samples at 5 mV s^{-1}. Each CV curve shows one redox couple. The anodic peaks are at around 0.3 V while the cathodic peaks are at around 0.5 V. The redox couples are corresponding to the faradic reaction of NiO which can be expressed by the following formula:[19,28]

$$NiO + OH^- \leftrightarrow NiOOH + e^- \quad (2)$$

GNO exhibits the smallest area surrounded by the CV curve, indicating the smallest specific capacitance. This results from

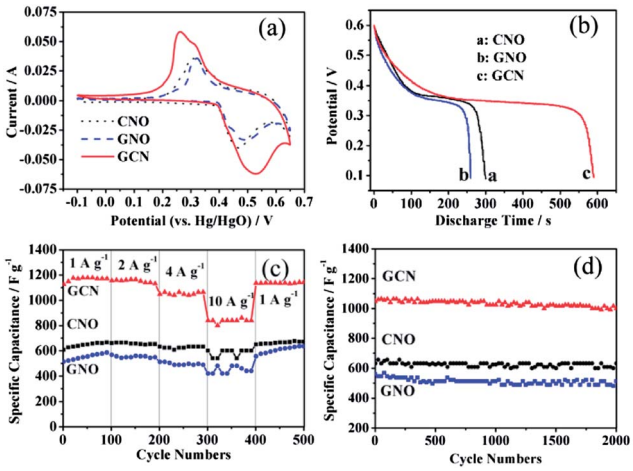

Fig. 6 (a) CV curves of CNO, GNO, and GCN electrodes at a scan rate of 5 mV s^{-1}. (b) The galvanostatic discharge curves of CNO, GNO, and GCN electrodes at 1 A g^{-1}. (c) Rate capacitance of CNO, GNO, and GCN electrodes with increasing current densities. (d) Cyclic performance of CNO, GNO, and GCN electrodes at 4 A g^{-1}.

the decreasing active sites caused by aggregation of RGO/NiO. The capacitance of CNO is enhanced a little compared with GNO. Nevertheless, NiO particles in CNO are large, which would also decrease the effective area for redox reactions. Therefore, the capacitance of CNO is not high, either. The CV curve of GCN is drastically expanded, implying an enhanced capacitance. Its improved capacitive properties are attributed to the uniform structure and high electrical conductivity. Fig. 6b displays the galvanostatic discharge curves of CNO, GNO, and GCN electrodes at a current density of 1 A g^{-1}. Consistent with the CV results, all samples show a typical pseudo-capacitive behavior with highly nonlinear discharge curves. It is believed that the discharge time is controlled by the rate of alkali ions diffusing into and out of the surface of the electrode.[27] The GCN electrode exhibits a much longer discharge time than the other two electrodes. The prolonged discharge time is attributed to increased redox reactions caused by the uniform structure and more active sites which correspond to the structural and morphological characterization as shown above.

To further analyze the electrochemical performance of CNO, GNO, and GCN electrodes, they were tested at different current densities. Fig. 6c displays the rate capacitance of CNO, GNO, and GCN electrodes with increasing current density. Under the same conditions, the specific capacitance of the GCN electrode is much higher than those of CNO and GNO electrodes. The GCN electrode takes the dual advantages of CNTs and RGO, leading to the great enhancement in capacitance. Not only is the conductivity improved by CNTs but also more active sites are contributed by smaller NiO on RGO. Through calculation, the specific capacitances at 1 A g^{-1} are 660, 580 and 1180 F g^{-1} for CNO, GNO, and GCN, respectively. The capacitance will decrease with the increase in current density. For the GCN electrode, the specific capacitance drops to 1050 F g^{-1} at 4 A g^{-1}, while the specific capacitances of CNO and GNO are only 630 and 490 F g^{-1} under similar conditions, respectively. Even at a high current density of 10 A g^{-1}, the specific capacitance of GCN is still as high as 840 F g^{-1}, which is much higher than those of CNO (600 F g^{-1}) and GNO (420 F g^{-1}). Fig. 6d displays the cyclability of CNO, GNO, and GCN electrodes at 4 A g^{-1}. The capacity retention ratios of CNO, GNO, and GCN are 95%, 87%, and 95%, respectively. The capacitance of GCN is still as high as 1000 F g^{-1} even after 2000 cycles, certifying excellent cycling stability.

Electrochemical impedance spectroscopy illustrates the electron transport properties of these samples. Fig. 7 shows the Nyquist plots of CNO (a), GNO (b) and GCN (c) electrodes. Each spectrum displays a depressed semicircle in the high-frequency region and a straight line in the low-frequency region. It is well accepted that the semicircle corresponds to the charge transfer resistance, which is related to the surface area and electrical conductivity.[49,50] The GCN electrode exhibits a smallest semicircle, indicating that the GCN electrode has lower charge transfer resistance than the other two electrodes, because tunnels for electron transport provided by CNTs and more available active sites decrease the charge transfer resistance. The straight line reflects the diffusion of the electro-active species.[51] The nearly vertical line indicates rapid ion diffusion into the electrolyte and adsorption onto the electrode surface.[52] CNO and GCN show nearly vertical shapes because electrons could transfer fast due to less aggregation and tunnels provided by CNTs. GNO exhibits the smallest slope of straight line, which corresponds to the limitation of ion diffusion caused by aggregated RGO/NiO sheets.

Based on the above electrochemical analysis, GCN showed excellent capacitive and cycling performance even at considerably high charge and discharge currents. The reason for this can be well understood if the following factors are considered. First, the aggregation of RGO coated with NiO is obviously lessened by the addition of CNTs, which could increase the effective area of GCN composites for redox reactions. The particle size of NiO is significantly reduced and more active sites are available in

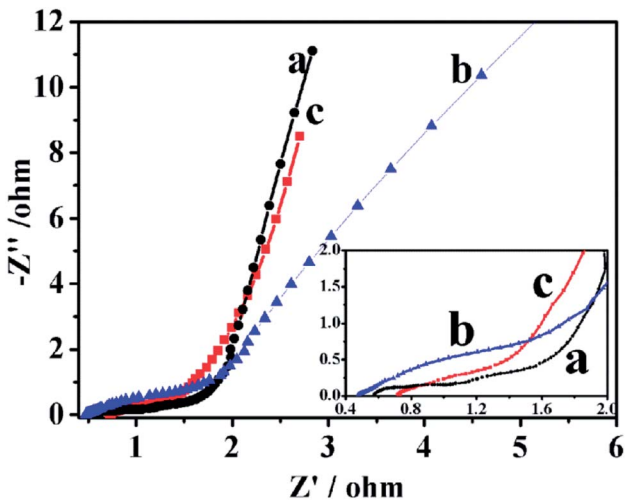

Fig. 7 Electrochemical impedance spectra (EIS) obtained from CNO (a), GNO (b) and GCN (c) electrodes. The inset shows the enlarged EIS of the electrodes.

redox reactions. Second, CNTs provide more tunnels for electron and ion transport to enhance the electric conductivity of the GCN electrode. Third, RGO and CNTs act as a structural buffer for the large volume expansion of NiO during the redox process. The unique architecture, high crystallinity, high conductivity and excellent dispersion state synergetically enhance the capacity and cycling performance of the GCN electrode.

4. Conclusions

We demonstrated an effective strategy for preventing the RGO/NiO from aggregation *via* a simple method under facile conditions. The addition of GNTs is the key factor that separates the RGO/NiO sheets. A high specific capacitance of 1180 F g^{-1} can be achieved for RGO/CNT/NiO composites. The excellent electrochemical performance is a result of the synergetic effect. NiO particles with high crystallinity and decreased particle size distribute homogenously on the RGO surface. The enhanced reduction degree of GO and tunnels for electron transport provided by CNTs improve the electron transport properties. Thus, GCN shows higher specific capacitance, better cyclicity and stability than those of CNO and GNO, which is promising for large-capacity energy storage.

Acknowledgements

This work is supported by the National Basic Research Program of China (2012CB932303) and the National Natural Science Foundation of China (Grant no. 51072215 and 51172261).

Notes and references

1 C. Y. Chen, C. Y. Fan, M. T. Lee and J. K. Chang, *J. Mater. Chem.*, 2012, **22**, 7697–7700.
2 H. S. C. H. Wang, Y. Liang and H. Dai, *J. Am. Chem. Soc.*, 2010, **132**, 7472–7477.
3 C. Liu, F. Li, L.-P. Ma and H.-M. Cheng, *Adv. Mater.*, 2010, **22**, E28–E62.
4 P. J. Sumanta Kumar Meher and G. Ranga Rao, *ACS Appl. Mater. Interfaces*, 2011, **3**, 2063–2073.
5 J. Z. Sheng Chen, X. Wu, Q. Han and X. Wang, *ACS Nano*, 2010, **4**, 2822–2830.
6 J. Liu, J. Jiang, C. Cheng, H. Li, J. Zhang, H. Gong and H. J. Fan, *Adv. Mater.*, 2011, **23**, 2076–2081.
7 S. P. M. D. Stoller, Y. Zhu, J. An and R. S. Ruoff, *Nano Lett.*, 2008, **8**, 3498–3502.
8 B. E. Conway, *Electrochemical Supercapacitors: Scientific Fundamentals and Technological Applications*, Plenum Publishers, New York, 1999.
9 X. Sun, G. Wang, J. Hwang and J. Lian, *J. Mater. Chem.*, 2011, **21**, 16581–16588.
10 Y. P. Zhai, Y. Q. Dou, D. Y. Zhao, P. F. Fulvio, R. T. Mayes and S. Dai, *Adv. Mater.*, 2011, **23**, 4828–4850.
11 N. Zhang, J. Sun, D. Jiang, T. Feng and Q. Li, *Carbon*, 2009, **47**, 1214–1219.
12 W. R. Zhong-Shuai Wu, D.-W. Wang, F. Li, B. Liu and H.-M. Cheng, *ACS Nano*, 2010, **4**, 5835–5842.
13 M. Noked, A. Soffer and D. Aurbach, *J. Solid State Electrochem.*, 2011, **15**, 1563–1578.
14 J. Li, W. Zhao, F. Huang, A. Manivannan and N. Wu, *Nanoscale*, 2011, **3**, 5103–5109.
15 Y. L. L. Liu, S. Yuan, M. Ge, M. Ren, C. Sun and Z. Zhou, *J. Phys. Chem. C*, 2010, **114**, 251–255.
16 C. Xu, X. Wang, J. Zhu, X. Yang and L. Lu, *J. Mater. Chem.*, 2008, **18**, 5625–5629.
17 X.-L. Huang, J. Chai, T. Jiang, Y.-J. Wei, G. Chen, W.-Q. Liu, D. Han, L. Niu, L. Wang and X.-B. Zhang, *J. Mater. Chem.*, 2012, **22**, 3404–3410.
18 R. B. Rakhi, W. Chen and H. N. Alshareef, *J. Mater. Chem.*, 2012, **22**, 5177–5183.
19 X. Zhang, W. Shi, J. Zhu, W. Zhao, J. Ma, S. Mhaisalkar, T. L. Maria, Y. Yang, H. Zhang, H. H. Hng and Q. Yan, *Nano Res.*, 2010, **3**, 643–652.
20 C.-Y. Cao, W. Guo, Z.-M. Cui, W.-G. Song and W. Cai, *J. Mater. Chem.*, 2011, **21**, 3204–3209.
21 H. Yang, G. H. Guai, C. Guo, Q. Song, S. P. Jiang, Y. Wang, W. Zhang and C. M. Li, *J. Phys. Chem. C*, 2011, **115**, 12209–12215.
22 X. Xia, J. Tu, Y. Mai, R. Chen, X. Wang, C. Gu and X. Zhao, *Chem. – Eur. J.*, 2011, **17**, 10898–10905.
23 P. Lin, Q. J. She, B. L. Hong, X. A. J. Liu, Y. N. Shi, Z. Shi, M. S. Zheng and Q. F. Dong, *J. Electrochem. Soc.*, 2010, **157**, A818–A823.
24 H. Y. Koo, H.-J. Lee, H.-A. Go, Y. B. Lee, T. S. Bae, J. K. Kim and W. S. Choi, *Chem. – Eur. J.*, 2011, **17**, 1214–1219.
25 D. Luo, G. Zhang, J. Liu and X. Sun, *J. Phys. Chem. C*, 2011, **115**, 11327–11335.
26 D. Chen, X. Wang, T. Liu, X. Wang and J. Li, *ACS Appl. Mater. Interfaces*, 2010, **2**, 2005–2011.
27 X. Zhu, H. Dai, J. Hu, L. Ding and L. Jiang, *J. Power Sources*, 2012, **203**, 243–249.
28 B. Zhao, J. Song, P. Liu, W. Xu, T. Fang, Z. Jiao, H. Zhang and Y. Jiang, *J. Mater. Chem.*, 2011, **21**, 18792–18798.
29 B. You, L. Wang, L. Yao and J. Yang, *Chem. Commun.*, 2013, **49**, 5016–5018.
30 H. Pan, J. Li and Y. Feng, *Nanoscale Res. Lett.*, 2010, **5**, 654–668.
31 Y. Zhai, Y. Dou, D. Zhao, P. F. Fulvio, R. T. Mayes and S. Dai, *Adv. Mater.*, 2011, **23**, 4828–4850.
32 Z. Fan, J. Chen, K. Cui, F. Sun, Y. Xu and Y. Kuang, *Electrochim. Acta*, 2007, **52**, 2959–2965.
33 W. S. Hummers Jr and R. E. Offeman, *J. Am. Chem. Soc.*, 1958, **80**, 1339.
34 H. Xia, Y. S. Meng, G. Yuan, C. Cui and L. Lu, *Electrochem. Solid-State Lett.*, 2012, **15**, A60–A63.
35 J.-B. Park, G.-S. Choi, Y.-S. Cho, S.-Y. Hong, D. Kima, S.-Y. Choi, J.-H. Lee and K.-I. Cho, *J. Cryst. Growth*, 2002, **244**, 211–217.
36 T. H. Yoon and Y. J. Park, *Nanoscale Res. Lett.*, 2012, **7**, 28–31.
37 B. Li, H. Cao, J. Yin, Y. A. Wu and J. H. Warner, *J. Mater. Chem.*, 2012, **22**, 1876.

38 Z. Gao, J. Wang, Z. Li, W. Yang, B. Wang, M. Hou, Y. He, Q. Liu, T. Mann, P. Yang, M. Zhang and L. Liu, *Chem. Mater.*, 2011, **23**, 3509–3516.
39 Y. Xu, K. Sheng, C. Li and G. Shi, *ACS Nano*, 2010, **4**(7), 4324–4330.
40 F. Yang, Y. Liu, L. Gao and J. Sun, *J. Phys. Chem. C*, 2010, **114**, 22085–22091.
41 C.-Y. Su, Y. Xu, W. Zhang, J. Zhao, X. Tang, C.-H. Tsai and L.-J. Li, *Chem. Mater.*, 2009, **21**, 5674–5680.
42 M. Li, J. E. Zhu, L. Zhang, X. Chen, H. Zhang, F. Zhang, S. Xu and D. G. Evansa, *Nanoscale*, 2011, **3**, 4240–4246.
43 H. Li, G. Zhu, Z.-H. Liu, Z. Yang and Z. Wang, *Carbon*, 2010, **48**, 4391–4396.
44 Z. Wen, X. Wang, S. Mao, Z. Bo, H. Kim, S. Cui, G. Lu, X. Feng and J. Chen, *Adv. Mater.*, 2012, **24**, 5610–5616.
45 Z. Tai, X. Yan and Q. Xue, *J. Power Sources*, 2012, **213**, 350–357.
46 Z. Ji, X. Shen, G. Zhu, H. Zhou and A. Yuan, *J. Mater. Chem.*, 2012, **22**, 3471–3478.
47 H. Hu, A. Yu, E. Kim, B. Zhao, M. E. Itkis, E. Bekyarova and R. C. Haddon, *J. Phys. Chem. B*, 2005, **109**, 11520–11524.
48 J. T. Chen, Y. J. Fu, Q. F. An, S. C. Lo, S. H. Huang, W. S. Hung, C. C. Hu, K. R. Lee and J. Y. Lai, *Nanoscale*, 2013, **5**, 9081–9088.
49 S.-E. Chun, S.-I. Pyun and G.-J. Lee, *Electrochim. Acta*, 2006, **51**, 6479–6486.
50 Y.-Y. Horng, Y.-C. Lu, Y.-K. Hsu, C.-C. Chen, L.-C. Chen and K.-H. Chen, *J. Power Sources*, 2010, **195**, 4418–4422.
51 L. Wang, Z. H. Dong, Z. G. Wang, F. X. Zhang and J. Jin, *Adv. Funct. Mater.*, 2013, **23**, 2758–2764.
52 M. Kim, Y. Hwang and J. Kim, *J. Power Sources*, 2013, **239**, 225–233.